

Highlights

A CFD-Based Investigation of Local Luminal Curvature as a Primary Determinant of Hemodynamic Environments in Cerebral Aneurysms

M. P. A. Dallavanzi, J.L. Gasche, I. L. Oliveira

- Local wall curvature is a robust, primary determinant of hemodynamics in intracranial aneurysms, independent of global flow patterns or rupture status.
- Saddle-like (hyperbolic) geometries preferentially exhibit high time-averaged wall shear stress (TAWSS) and low oscillatory shear index (OSI) driven by intense near-wall vortical activity.
- Spherical-like (elliptic) geometries are dominated by flow impingement and stagnation, leading to elevated oscillatory shear and lower shear stress.

A CFD-Based Investigation of Local Luminal Curvature as a Primary Determinant of Hemodynamic Environments in Cerebral Aneurysms

M. P. A. Dallavanzi^b, J.L. Gasche^c, I. L. Oliveira^{a,*}

^a*São Paulo State University (UNESP), School of Engineering, Bauru, Department of Mechanical Engineering. Av. Engenheiro Luiz Edmundo Carrijo Coube, 14-01, 17033-360, Bauru, SP, Brazil*

^b*São Paulo State University (UNESP), School of Engineering, Bauru, Department of Mechanical Engineering.*

^c*São Paulo State University (UNESP), School of Engineering, Ilha Solteira, Mechanical Engineering Department*

Abstract

The relationship between vascular morphology and hemodynamics is important to understanding the natural history of cerebral aneurysms (CAs). While global geometric indices have been widely studied, the local interaction between luminal curvature and wall shear stress (WSS) remains poorly characterized. This study analyzed a large, heterogeneous cohort of patient-specific CAs to investigate how local surface morphology is related to hemodynamic environments. This was performed via Computational Fluid Dynamics flow simulations of a set of 76 patient-specific CAs geometries using the OpenFOAM[®] library. Geometry and patient-specific pulsatile inflow conditions were modeled based on the patient arterial diameter and age. Blood was assumed as

*Corresponding author

Email addresses: marcella.avanzi@unesp.br (M. P. A. Dallavanzi),
jose.gasche@unesp.br (J.L. Gasche), iago.oliveira@unesp.br (I. L. Oliveira)

a Newtonian incompressible fluid flowing in a laminar regime. We utilized a geometric framework to classify the aneurysm lumen into spherical-like (elliptic) and saddle-like (hyperbolic) patches based on Gaussian curvature. Our results demonstrate a robust, statistically significant correlation between these curvature types and hemodynamic metrics, regardless of rupture status or aneurysm type. Specifically, saddle-like patches, predominantly found at the aneurysm neck, are associated with high time-averaged wall shear stress, low oscillatory shear index, and intense near-wall vortical activity as identified by the λ_2 -criterion. In contrast, spherical-like patches, dominant at the dome, correspond to regions of flow impingement characterized by lower time-averaged wall shear stress and elevated oscillatory shear index. These findings suggest that wall curvature is a primary determinant of local hemodynamics, overriding variations in global flow patterns. By bridging the gap between wall local morphology and pathological wall markers, this work suggests curvature-based mapping can serve as a powerful tool for identifying vulnerable regions susceptible to thinning and rupture. This objective geometric assessment offers valuable insights for risk stratification and the precision planning of endovascular interventions.

Keywords: Intracranial aneurysms, Wall curvature, Hemodynamics, Computational Fluid Dynamics, OpenFOAM[®]

1. Introduction

The rupture of a cerebral aneurysm (CA) — pathological dilatations of the arterial tree supplying the brain — remains a severe neurovascular problem associated with high risks of mortality and morbidity [1, 2]. While therapeutic

interventions exist, their significant procedural risks force neurosurgeons into a complex decision-making process between intervention and conservative longitudinal monitoring. Currently, clinical management relies on patient-specific factors — such as age, sex, family history, comorbidities, and smoking status — alongside fundamental geometric metrics — aneurysm sac diameter and height — and anatomical location [3]. Qualitative morphological features, including “blebs” or lobular regions, are also considered due to their strong association with increased rupture risk [4, 5, 6]. However, the final clinical assessment often remains inconclusive. Elaborated scoring systems have been developed to provide objective guidance [7, 8, 9]. For example, Etminan et al. [10] proposed the “unruptured CA treatment score” score based on 29 clinical, morphologic and geometric factors. However, an evaluation by Rajabzadeh-Oghaz et al. [11] demonstrated that 43% of cases were classified as non-definitive. This high rate of ambiguity suggests that established scoring criteria may be insufficient for a final clinical decision and underscores the necessity to incorporate additional factors.

Extensive research suggests that the initiation, development, and eventual rupture of CAs are primarily driven by hemodynamic forces acting on the vessel lumen [12, 13, 14], implying that hemodynamic data should be incorporated into clinical scores. However, the specific mechanisms governing aneurysm progression remain debated [6]. To investigate these, Computational Fluid Dynamics (CFD) has become a standard tool for simulating blood flow within both idealized and patient-specific vascular networks, elucidating variables linked to aneurysm evolution [15, 16]. Recent investigations have shifted toward granular descriptions of intra-aneurysmal flow [17, 18] and

localized phenomena like bleb and thrombus formations, which are intimately connected with specific near-wall flow environments [19, 20]. Nevertheless, implementing CFD in routine practice is restricted by high computational costs, the time-to-result for high-fidelity simulations, and the need for specialized expertise. Consequently, proxies for intra-aneurysmal flow would be valuable for faster, more accessible clinical assessments.

Morphological changes, such as blebs and thrombi, alter the luminal curvature — an important mathematical determinant of wall stress [21, 22]. Recent research has further highlighted the role of curvature in shaping wall stress and local hemodynamics. Oliveira et al. [23] demonstrated that specific curvature types correlate with abnormal flow conditions known to drive aneurysm growth, rupture, and tissue degradation [24, 25]. The present study expands the current understanding by investigating the relationship between wall curvature and hemodynamics in a robust, larger cohort. To this end, we conducted CFD simulations across 76 patient-specific CAs under realistic boundary conditions. Our analysis elucidates the correlations between curvature metrics and hemodynamic variables while pinpointing the specific flow structures within the aneurysm sac that drive these pathological signatures. If luminal curvature dictates local hemodynamics, it represents a promising candidate for clinical scoring systems, offering an objective metric for features currently assessed only qualitatively.

2. Numerical Methodology

2.1. Geometries of Patient-specific Aneurysms

Patient-specific CA geometries were obtained from the *Aneurisk* repository [26], which provides 100 cases under a “Creative Commons” license. From this dataset, 76 cases from the anterior circulation (including internal carotid artery, middle cerebral artery, and anterior cerebral artery) were selected. The exclusion criteria were: (i) arterial trees with multiple aneurysms; (ii) models where outlets were positioned too close to the aneurysm sac to ensure accurate boundary condition application; and (iii) internal carotid artery lengths insufficient for consistent clipping.

The geometries in the *Aneurisk* repository often include extensive arterial segments beyond the region of interest. To avoid operator bias during inlet selection, we employed an automated clipping procedure. Surfaces were clipped at the fourth internal carotid artery bend, identified using the curvature and torsion-based classification by Piccinelli et al. [27]. This standardized approach ensures that flow inlets are consistently positioned across all cases, following the methodological recommendations of Valen-Sendstad et al. [28].

2.2. Physical Modeling of the Blood Flow and Boundary Conditions

Blood flow was computed assuming rigid walls (Fig. 1a) and an incompressible, Newtonian fluid model under isothermal conditions. The continuity equation:

$$\nabla \cdot \mathbf{v} = 0, \tag{1}$$

and the Navier-Stokes equations for constant viscosity:

$$\frac{\partial(\rho\mathbf{v})}{\partial t} + \nabla \cdot (\rho\mathbf{v}\mathbf{v}) = -\nabla p + \mu\nabla^2\mathbf{v}, \quad (2)$$

governing the fluid flow were numerically solved for the velocity, \mathbf{v} , and pressure, p , fields. Blood was characterized by a density (ρ) of 1056 kg/m³ and dynamic viscosity (μ) of 3.5×10^{-3} Pa s [29, 30].

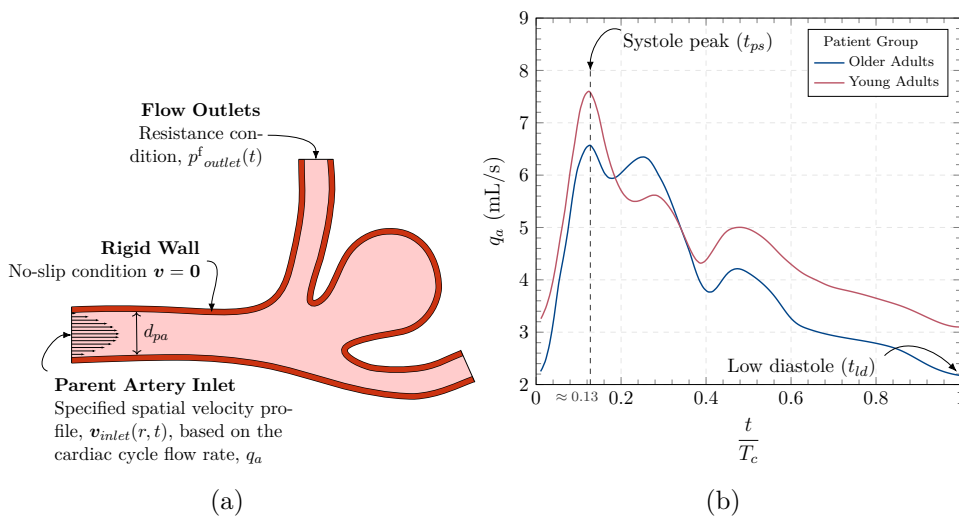


Figure 1: (a) Schematic example of the domain representing the blood flow through a typical CA. (b) Population-averaged inflow rate waveforms used in the simulations for young adults, after data taken from Ford et al. [31], and older adults, after data taken from Hoi et al. [32] (time axis normalized by the cardiac period, T_c , of each profile).

As the flow through the real intracranial arteries is already developed, at the flow inlets, we imposed a spatially-varying pulsatile velocity profile according to the fully-developed laminar flow in a straight pipe:

$$\mathbf{v}_{inlet}(r, t) = 2 \frac{q_p(t)}{A_{inlet}} \left[1 - \frac{4r^2}{d_{pa}^2} \right], \quad (3)$$

where A_{inlet} is the cross-sectional area of the inlet artery, d_{pa} is its inner diameter, and r is the radial coordinate of the circular inlet section. To avoid artificial recirculation at the model inlet, as they are not circular, an artificial circular-section extension, with a length equal to twice the diameter d_{pa} , was added to the artery inlet to impose this inlet flow condition. The blood flow rate, $q_p(t)$, was determined based on the geometry inlet diameter and the patient age, available in the *Aneurisk* repository data, to utilize inflow boundary conditions as closely as possible with patient-specific ones. As proposed by Valen-Sendstad et al. [28], it was computed as follows:

$$q_p(t) = q_a(t) \left(\frac{d_{pa}}{d_{avg}} \right)^2, \quad (4)$$

where d_{pa} is the diameter of the patient’s internal carotid artery at the inlet (see Fig. 1a) and the square power was recommended by Valen-Sendstad et al. [28] for cerebral arteries — rather than the cube power predicted by Murray’s law. The population-average diameter of the internal carotid artery, d_{avg} , was the sample’s internal carotid artery average diameter at the truncated location, yielding a value of 4.35 mm. The populational-averaged flow rate waveform, q_a , was selected according to the patient’s age. The profiles measured at the cerebral arteries for “older adults” by Hoi et al. [32], who measured blood flow rates in patients with an average age of 68 ± 8 years, and for “young adults” by Ford et al. [31], who conducted similar measurements in patients with an average age of 28 ± 7 years (see Fig. 1b). Based on these thresholds, the sample cases were categorized into “older adults”, age ≥ 50 years, and “young adults”, age < 50 years. The threshold of 50 years was selected as an approximation of the average age separating these two groups.

Additionally, zero-pressure gradient was applied at the inlet. At the vascular outlets, a flux-corrected zero-gradient condition was employed for the velocity, and a resistance condition, where the outlet pressure is proportional to the flow profile over time [33], was applied for the pressure (Fig. 1b).

2.3. Numerical Strategies

Equations (1) and (2) were numerically solved using OpenFOAM[®] (v23.12). To maintain second-order accuracy, we employed a second-order upwind scheme for advective terms, the Green-Gauss scheme for velocity and pressure gradients, and second-order central differences for diffusion terms — incorporating non-orthogonal and skewness corrections [34]. Pressure-velocity coupling was managed via the PISO algorithm [35].

Computational meshes were generated with **snappyHexMesh**, resulting in predominantly hexahedral cells. The mesh conforms to the curved lumen boundary using polyhedral cells at the wall, supported by a five-layer prismatic boundary-layer refinement. Elements were designed to refine progressively toward the wall. Based on extensive mesh and time-step sensitivity studies across various CAs geometries, we adopted an optimal cell density of, at least, 3000 cells/mm³ and the temporal discretization utilized a fixed time-step of 1×10^{-4} s [36]. To eliminate initial transient effects, three cardiac cycles were simulated, with only the final cycle retained for hemodynamic analysis.

2.4. Data Analysis

Subdivisions of the Aneurysm Sac Surface by Local Shape

The aneurysm sac surface was partitioned using two patching schemes. First, we used the Gaussian curvature (K) to classify surface topology [37, 23].

At any given point on a surface, the Gaussian curvature is defined as the product of the two principal curvatures that represent the maximum and minimum normal curvatures at that point. Gaussian curvature fields, measured in mm^{-2} , were computed in Visualization Toolkit (VTK)[®] and classified with an in-house Python code (see Fig. 2a for an example on case C0001 of the Aneurisk database). Gaussian curvature categorizes regions as elliptic ($K > 0$, ellipsoidal), parabolic ($K = 0$, cylindrical), or hyperbolic ($K < 0$, saddle-shaped) (see Fig. 2b where we included a detail of a typical shape of saddle and elliptical surfaces). Our mapping focused on morphologically relevant classes found in the vascular sample [37] — saddle and ellipsoidal-shaped —, excluding physiologically improbable types like perfectly planar surfaces that were not identified. For simplicity, in our discussions, we refer to elliptic regions as “spherical-like” and hyperbolic regions as “saddle-like”.

Second, the sac was divided into clinically relevant regions: “neck”, “body”, and “dome”. Following Salimi Ashkezari et al. [38], we calculated the geodesic distance from the neck contour, g_n , using VTK[®]. The aneurysm sac surface was partitioned based on the maximum geodesic distance, $g_{n,max}$, and categorized as *neck* for g_n up to $0.20g_{n,max}$, *body* for values between $0.20g_{n,max}$ and $0.60g_{n,max}$, and the *dome* for distances exceeding $0.60g_{n,max}$ (see Fig. 2c).

2.5. Hemodynamics and Flow Characterization

From the CFD results, our analysis proceeded in two parts. First, we focused on hemodynamic quantities derived from the wall shear stress (WSS) vector, $\boldsymbol{\tau}_w$ (bold-face font for vectors). We computed the time-averaged wall shear stress (TAWSS), defined as the temporal average of the WSS magnitude,

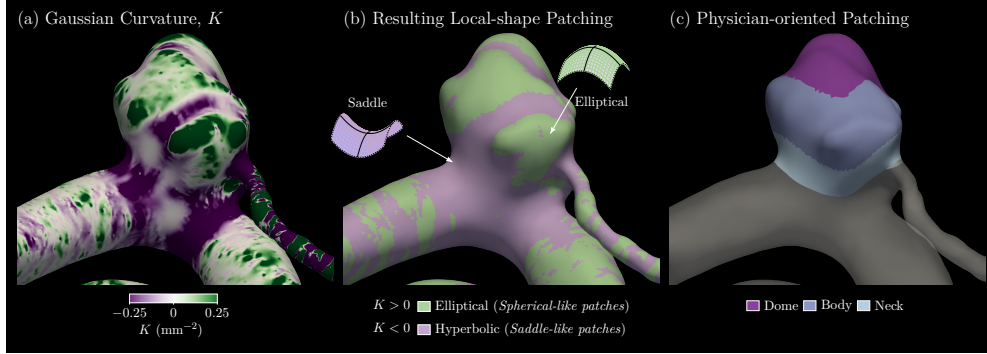


Figure 2: Example, for case C0001 of the Aneurisk repository, of the (a) Gaussian, K , curvature fields of the lumen surface, and (b) the resulting local-shape patching, based on the one proposed by Ma et al. [37], depicted at the bottom of the panel in a tabular format, with an illustration of what shape each surface has, and (c) the neck, body, and dome patches (figure adapted from Oliveira et al. [23]).

τ_w (no bold-face font for magnitudes):

$$TAWSS = \frac{1}{T_c} \int_0^{T_c} \tau_w dt, \quad (5)$$

where T_c is the cardiac period. Additionally, we calculated the oscillatory shear index (OSI), which quantifies the temporal variation in the direction of the WSS vector [39]:

$$OSI = \frac{1}{2} \left(1 - \frac{\left\| \frac{1}{T_c} \int_0^{T_c} \boldsymbol{\tau}_w(\mathbf{x}, t) dt \right\|}{\frac{1}{T_c} \int_0^{T_c} \|\boldsymbol{\tau}_w(\mathbf{x}, t)\| dt} \right). \quad (6)$$

We also computed and analyzed the time-averaged WSS gradient (TAWSSG) as defined in Geers et al. [15] to quantify spatial gradients of TAWSS. Its definition and calculation are detailed in the Supplementary Material.

Second, to characterize intra-aneurysmal flow and its impact on the wall, we identified fixed points of the cycle-averaged WSS vector field [40]. In this

context, fixed points — namely, saddles, foci and nodes — are locations where the WSS vector vanishes, effectively representing stagnation points where the near-wall velocity is zero [41, 42]. These points mark the origin or termination of separation and impingement lines [43], referred to as *flow separatrices*. These trajectories were computed by integrating the cycle-averaged WSS vector field on the lumen surface [44]. Fig. 3 illustrates some fixed point topologies observed in this study, although other topologies may occur. For the sake of clarity, we adopt the terms “separation” and “impingement” rather than standard dynamical systems nomenclature, as can be seen in Fig. 3.

Complementing this, we used an Eulerian approach based on the divergence of the normalized cycle-averaged WSS field to identify regions of flow approaching or leaving the wall [46, 43, 44]:

$$\text{divWSS} \equiv \nabla \cdot \left(\frac{\overline{\boldsymbol{\tau}_w}}{\|\overline{\boldsymbol{\tau}_w}\|} \right), \quad (7)$$

Physically, positive divWSS characterizes impingement zones where flow

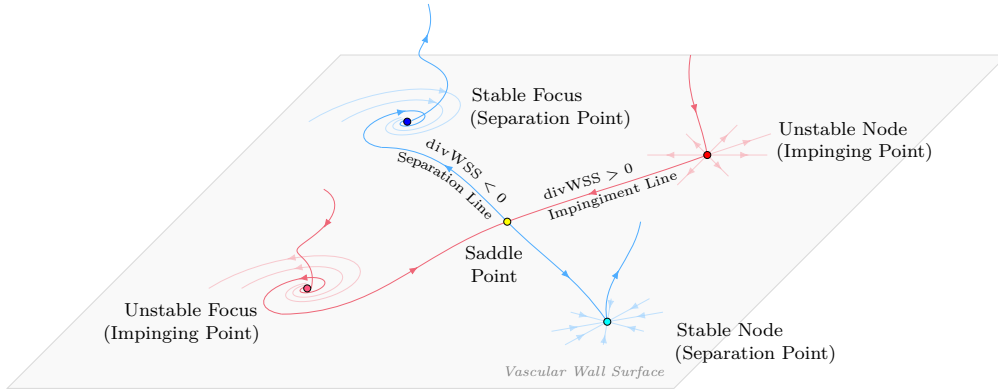


Figure 3: Schematic representation of the fixed points topology of the cycle-averaged WSS vector field. Arrows indicate lines of flow separation or impingement originating from or terminating at these points (inspired by figures in Surana et al. [43], Mazzi et al. [45]).

directed toward the wall is forced to spread laterally occurring around a impingement line. Conversely, negative divWSS identifies separation regions, capturing regions where the flow is leaving the luminal surface and around a separation line, as illustrated in Fig. 3.

2.6. Statistical Analysis

Statistical analysis was conducted on $n = 76$ aneurysm cases using the SciPy library [47] with a significance level of $\alpha = 0.05$. Normality was assessed via the Shapiro-Wilk test. To compare metrics between ruptured and unruptured cases, lateral and bifurcation aneurysms, and across different patch types, we employed paired t-tests for normally distributed data and Wilcoxon signed-rank tests for non-normal distributions.

The statistical analysis was performed on the surface-averaged metric for the TAWSS, OSI, and divWSS across each patch. The surface average of a field F was defined as:

$$\langle F \rangle_{S_i} = \frac{1}{A(S_i)} \int_{S_i} F dS_i, \quad (8)$$

where $A(S_i)$ denotes the surface area of the specific saddle-like or spherical-like patches identified in Fig. 2b.

3. Results

Aneurysm Sac Patches Characterization

To evaluate the morphological composition of the aneurysm wall, we categorized the surface into discrete patches based on local curvature properties.

This section details the prevalence and spatial distribution of these patches across the aneurysm sac, as summarized in Fig. 4. Spherical-like patches are more prevalent on CA sacs, while saddle-like patches occupy 30 to 45 % of the surface area and spherical-like are, on average, 56.7 % larger ($p < 0.001$). These area distributions do not differ significantly between ruptured and unruptured aneurysms (see p -values in Fig. 4a).

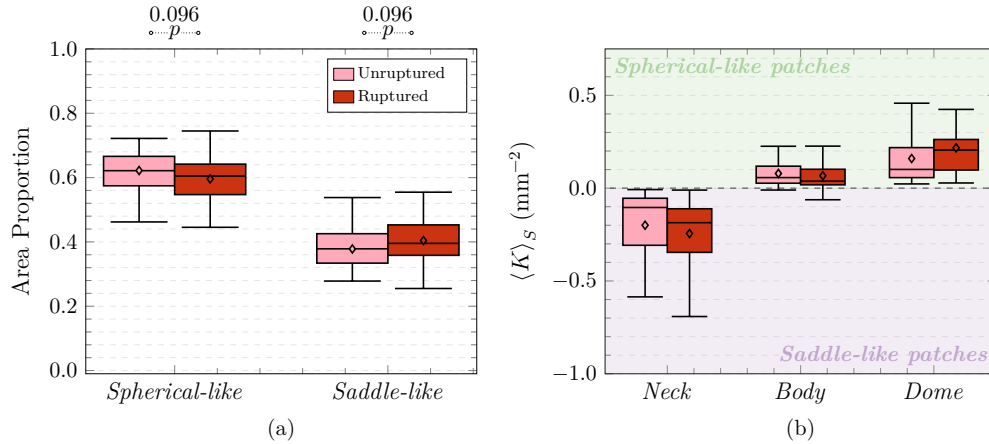


Figure 4: Distributions of (a) surface area percentage of curvature patches relative to the total aneurysm area and (b) surface-averaged Gaussian curvature across neck, body, and dome regions.

The distributions of $\langle K \rangle$ for physician-oriented patching (Fig. 4b) reveal distinct morphological patterns. Neck patches are characterized by negative Gaussian curvature, identifying them as predominantly saddle-like. In contrast, aneurysm domes are primarily composed of spherical-like patches, whereas the body patches exhibit intermediate morphological characteristics between these two extremes. This pattern can be noticed by the example of case C0001 comparing Fig. 2a and c.

Local Hemodynamics on Saddle-like and Spherical-like Patches

Hemodynamic data from the Aneurisk repository reveal that TAWSS was significantly higher on saddle-like patches compared to spherical-like regions ($p \ll 0.001$, Fig. 5a), with an average increase of 55.7%. Conversely, OSI exhibited the opposite trend, averaging 15.0% lower on saddle-like patches ($p \ll 0.001$, Fig. 5b). Notably, the difference in rupture resemblance score (RRS) — a parameter correlated with OSI that identifies local flow recirculation near the lumen — was even more pronounced; saddle-like patches presented an average RRS 95.5% lower than spherical-like patches. Furthermore, the *TAWSSG* showed significantly higher dispersion on saddle-like regions, with a standard deviation 3.4 times larger than on spherical-like patches (data provided in Supplementary Material). This suggests that TAWSS on spherical-like surfaces is more spatially uniform along the flow direction than on saddle-like surfaces. No significant differences were observed in any hemodynamic parameters when comparing saddle-like or spherical-like patches between ruptured and unruptured subgroups (p -values shown in Fig. 5). Similarly, no significant variations were detected when comparing lateral and bifurcation cases within each patch type (data not shown).

A representative example of these hemodynamic patterns is seen in case C0002 (Fig. 6), a lateral aneurysm with a balanced distribution of saddle-like and spherical-like regions. As shown in Fig. 6b, TAWSS is high near the neck (point A), characterized by saddle-like geometry, but decreases as the flow enters the sac and passes through another saddle-like region (point B). This results in reduced TAWSS within the spherical-like region of the dome. In contrast, the OSI field (Fig. 6c) is elevated in the dome, coinciding with

spherical-like patches, while lower values are maintained on saddle-like patches near the neck and body.

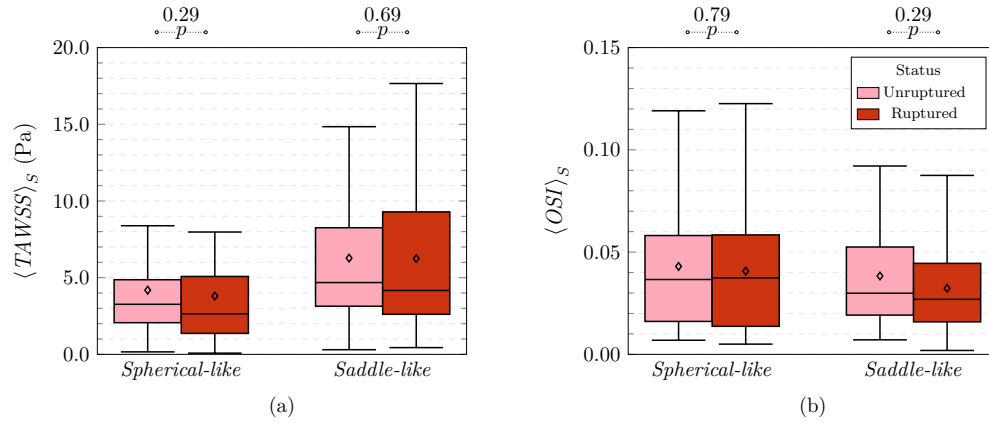


Figure 5: Distributions of (a) $\langle TAWSS \rangle_s$ and (b) $\langle OSI \rangle_s$ across spherical-like and saddle-like patches, with the sample segregated by rupture status.

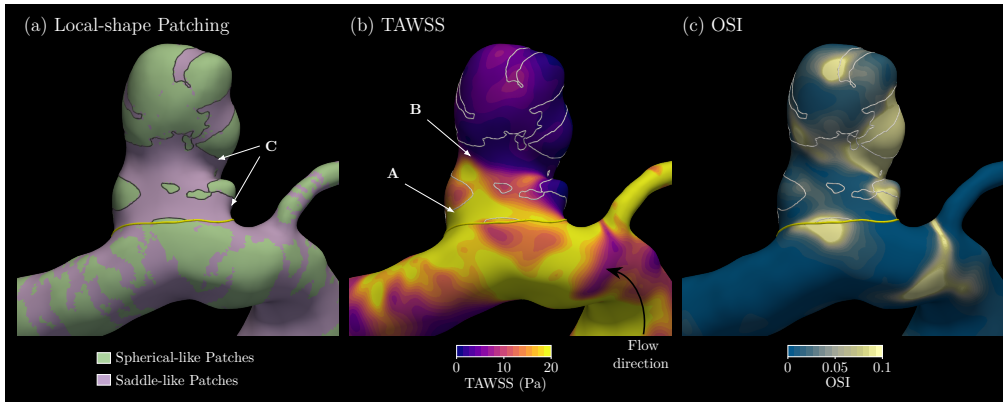


Figure 6: Local hemodynamics in a representative lateral aneurysm (case C0002): (a) local shape patching, (b) TAWSS field, and (c) OSI field (the yellow line marks the aneurysm neck).

Correlation between Hemodynamics and Wall Curvatures

The definitions of spherical-like and saddle-like patches are rooted in the Gaussian curvature of the lumen. The results in Fig. 5 suggest a correlation between local hemodynamics and these morphological metrics. Our analysis confirms a distinct correlation between selected hemodynamic parameters and Gaussian curvature, as the data in Fig. 7 reveals. Specifically, regions with increasingly negative Gaussian curvature tend to exhibit higher TAWSS, lower OSI (Fig. 7a and c), and higher, more positive TAWSSG (see Supplementary Material). These conditions suggest that on saddle-like patches, high and growing TAWSS occurs in conjunction with a constant WSS vector direction that does not undergo significant rotation during the cardiac cycle. Areas of pronounced negative Gaussian curvature correspond to surfaces that are more sharply curved in the two principal directions, as exemplified by the “squeezed” saddle topology at region C in Fig. 6.

These correlations invert on spherical-like patches. In these regions, TAWSS increases and OSI decreases as curvature increases, though the sensitivity of OSI to curvature is less pronounced than on saddle-like patches (Fig. 7b and d). While TAWSSG is slightly positively correlated with curvature on spherical-like surfaces, its average remains much closer to zero and is statistically distinct from the values observed on saddle-like patches (see Supplementary Material).

Wall Adjacent Flow Causing Hemodynamic Patterns

To interpret these hemodynamic patterns, it is essential to identify the underlying 3D flow structures adjacent to the lumen. High WSS regions are

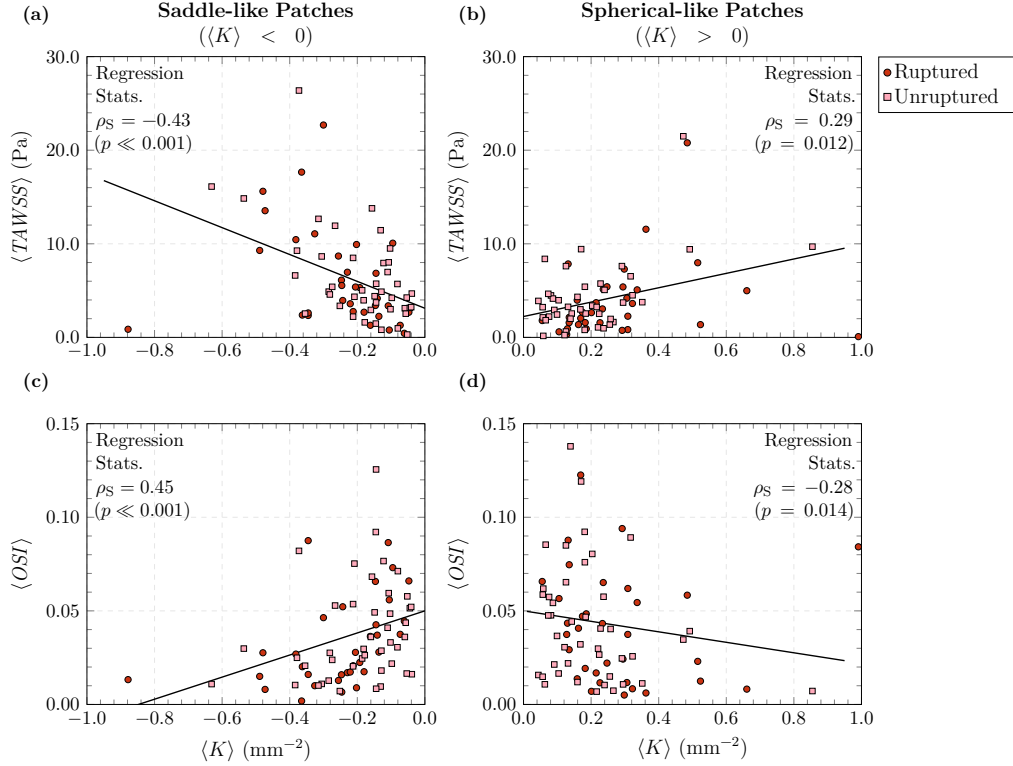


Figure 7: Correlation between $\langle TAWSS \rangle$ (a, b) and $\langle OSI \rangle$ (c, d) versus $\langle K \rangle$ across spherical and saddle-like patches, segregated by rupture status. (Spearman's correlation coefficients and p-values annotated were computed with SciPy)

fundamentally linked to high wall vorticity, ζ , as described by the relationship at at no-slip boundaries [46]:

$$\tau_w = \mu (\zeta \times \hat{n}) \quad (9)$$

where \hat{n} is the outward unit normal vector. Additionally, given that vortices are typically generated in regions of flow impingement and separation, the WSS vector field on an aneurysm sac is rarely unidirectional. Consequently, OSI levels (Eq. (6)) tend to be higher where the adjacent flow departs from a

unidirectional path. To determine if this behavior predominates over spherical-like patches, we examined markers of flow separation and attachment.

Using case C0002 as a representative example (Fig. 8), we observe flow originating from the internal carotid artery sweeping across the aneurysm neck. This generates a region of positive divWSS and high TAWSS (point A in Fig. 6b), where an attachment line crosses the neck (Fig. 8b). As the flow enters the sac, it separates from the wall at a separation line terminating at a separation point (stable node) near the dome. These regions are marked by negative $\overline{\lambda}_2$ values, indicating intense near-wall vorticity responsible for the elevated TAWSS (Fig. 8c; this can also be confirmed in the Supplementary Material where we present the temporal evolution of the λ_2 field and the WSS with a video and a figure).

This pattern is consistent across the sample. In lateral aneurysms, the inflow typically surrounds the wall, forming a vortex at a separation focus

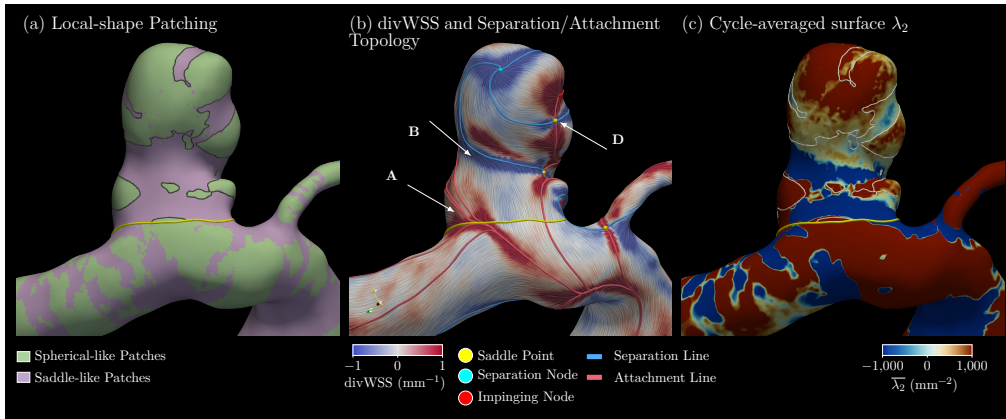


Figure 8: Flow characterization in case C0002: (a) curvature patch type; (b) divWSS with surface limiting streamlines (of the cycle-averaged WSS vector field with the line-integral convolution technique), fixed points, and separatrix lines; (c) cycle-averaged λ_2 field on the vascular surface (the yellow line marks the aneurysm neck).

or node, often on the dome. This stream may impinge on the dome (see impinging node on the region of positive WSS divergence in Fig. 8b) before detaching at a separation line that originates at a saddle point near the neck or body (an example can be seen in point D in Fig. 8b). In bifurcation aneurysms, the behavior is more complex and, by inspection of the bifurcation cases in the sample, seems to depend on the aneurysm orientation relative to the parent artery. However, inflow jets frequently impinge on the dome, producing an impinging node and a subsequent separation line where the jet meets the circulating flow. The relationship between these flow features and the underlying wall morphology are supported by the distribution of fixed point types, where saddle points, separation foci, and impinging nodes are the most prevalent features as can be seen in Fig. 9, showing the joint probability distribution of the fixed points. The joint probability represents the likelihood of a specific fixed-point type occurring concurrently with a specific curvature patch, effectively identifying a topological flow structure to the local geometry.

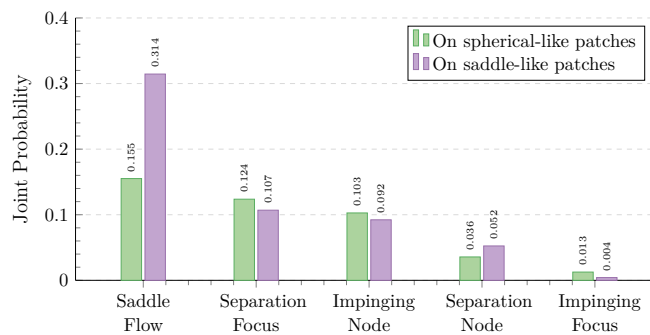


Figure 9: Distribution, measured by the probability of occurrence, of fixed point types across different curvature patches.

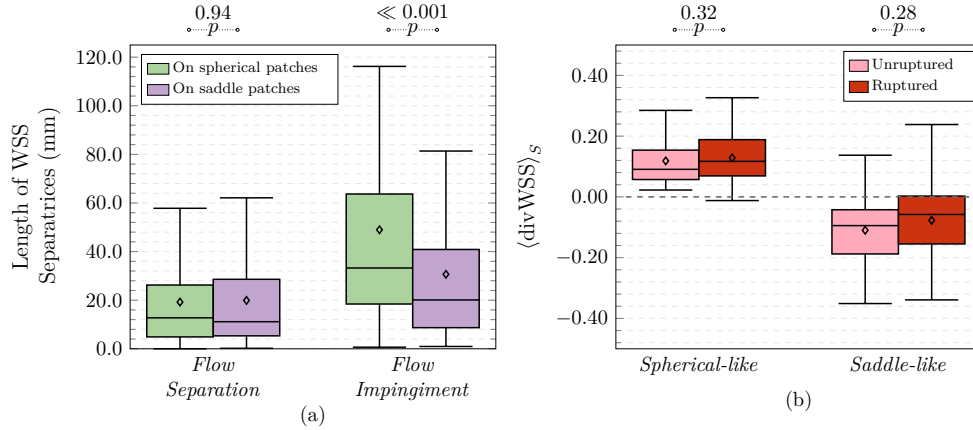


Figure 10: (a) Distribution of impingement and separation line lengths by patch type. Only aneurysmal flow features are included. (b) Box plots of the divWSS distributions by patch type and rupture status.

Analysis of separatrix lengths (see Fig. 10a) further reveals that spherical-like patches are more likely to exhibit longer impingement lines than saddle-like patches. Specifically, on spherical-like patches, impingement lines are approximately 155% longer than separation lines. This aligns with the observed positive WSS divergence on these patches (see Fig. 10b), indicating that impinging flow dominates the more spherical dome regions. The prevalence of these structures explains the higher OSI values observed in spherical-like regions, where the instantaneous WSS vector fluctuates significantly due to the impinging flow.

Impingement lines are also significantly longer on saddle-like patches ($p \ll 0.001$) by 54.0%, on average. Indeed, regions of positive divWSS are prevalent on these patches (Fig. 10b), supporting our previous observation that the sweeping inflow stream first encounters saddle-like geometry near the neck. Nevertheless, negative WSS divergence — a marker of flow moving

away from the wall — is also common on saddle-like patches. This is likely explained by regions of vortex formation that coincide with negative λ_2 values, as demonstrated in case C0002 (see Fig. 8c). Furthermore, the regions of higher TAWSS coincide with negative λ_2 (comparing Fig. 6b and Fig. 8c). Previous works have established a relationship between near-boundary vortical activity and WSS peaks. El Hassan et al. [48] found that vortical structures advected from a jet shear layer correlated with the location of WSS peaks at the wall. Similarly, Wild et al. [49] identified hairpin vortices in the carotid bifurcation responsible for high wall shear stress. Therefore, it is reasonable to conclude that the elevated TAWSS on saddle-like patches is primarily due to the formation of vortices adjacent to these regions, identified by negative λ_2 values in areas of detaching flow.

Finally, regions of negative λ_2 are most commonly found on hyperbolic (saddle-like) patches as supported by our data (Fig. 11), where the correlation between surface-averaged λ_2 and divWSS is statistically significant ($p \ll 0.001$) for both patch types. Most importantly, the results indicate that spherical-like patches tend to be adjacent to flow with positive λ_2 and positive divWSS ; here, the flow is dominantly impinging with low TAWSS due to minimal near-wall vortical activity. In contrast, flow on saddle-like patches is more likely to exhibit negative average λ_2 and high-intensity vorticity, marking regions of detaching flow and elevated shear stress.

4. Discussion

Our findings elucidate critical aspects of hemodynamics within a relatively large cohort of CAs. First, our results corroborate the hypothesis proposed by

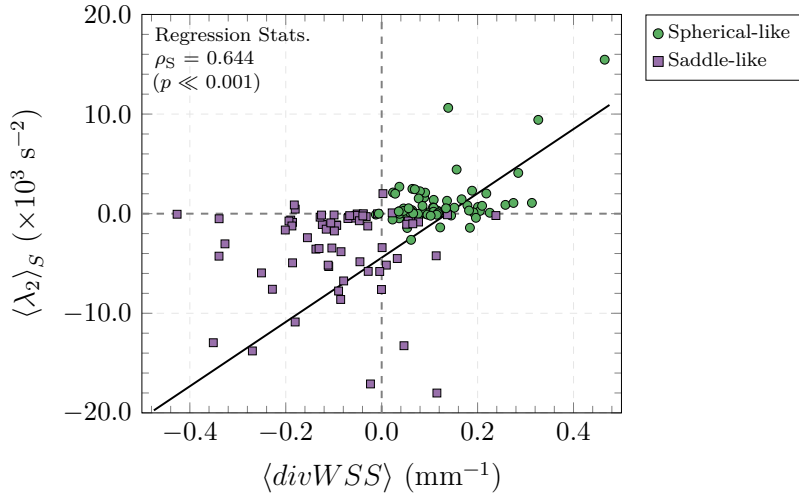


Figure 11: Correlation plot between surface-averages of λ_2 and $\text{div}WSS$ categorized by patch type (Spearman’s correlation coefficient and p-value annotated were computed with SciPy).

Oliveira et al. [23]: a clear relationship exists between luminal curvature and local hemodynamics that is maintained across a broad sample. Notably, these correlations persist across sub-samples categorized by rupture status and aneurysm type (lateral or bifurcation). This is particularly significant because inflow patterns differ substantially between these types; lateral aneurysms typically feature a single main vortex, while bifurcation aneurysms exhibit complex patterns with multiple vortices. Thus, the relationship between curvature and hemodynamics appears robust to variations in global flow topology. Furthermore, these findings were obtained using patient-specific boundary conditions, with flow rates scaled by vessel diameter and patient age, further strengthening the results.

Our results align with previous studies characterizing the hemodynamic environments of intracranial aneurysms. In a large-scale analysis, Karnam

et al. [20] reported low WSS and high OSI on the aneurysm dome, contrasted by high WSS and low OSI primarily at the neck. While their study did not explicitly incorporate wall curvature, their anatomical findings are consistent with our geometric framework, given that the dome is predominantly composed of spherical-like patches, whereas the neck consists mainly of saddle-like patches. Furthermore, Varble et al. [50] investigated vortical activity within the aneurysm sac using the Q-criterion [46] — a method analogous to the λ_2 -criterion employed in our analysis. They observed that high WSS values occurred in regions of positive Q, which identify vortical structures adjacent to the wall, further supporting our observation that near-wall vorticity drives elevated shear stress.

Abnormal hemodynamic conditions are known to trigger biological cascades in vessel tissue. Specifically, the inception of CAs has been linked to elevated WSS and high, positive TAWSSG [51, 25]. These conditions occur naturally at vascular bifurcations due to flow impingement, where the apex is characterized by saddle-like points. Frösen et al. [25] described an “inflammation-mediated” pathway for CA inception, highlighting a feedback loop that may continue even if WSS reestablishes baseline levels. Our findings suggest that WSS may remain elevated due to the saddle-like nature of the initial bulge at the neck, potentially reinforcing this inflammatory pathway.

While there is consensus on CA inception, the mechanisms governing subsequent growth remain a subject of debate. Meng et al. [24] proposed a “high-flow” pathway, where high WSS, positive gradients, and low OSI degrade the wall matrix, leading to thin-walled blebs. Conversely, a “low-flow” environment (low TAWSS and high OSI) may trigger an inflammatory

response leading to thick, atherosclerotic walls — the “low-flow” pathway [52, 53]. Our results suggest preferential locations for these events: saddle-like (hyperbolic) patches favor high-flow conditions, while spherical-like (elliptic) patches favor low-flow conditions.

Furthermore, using the terminology of Meng et al. [24], high-flow conditions are often assumed to be synonymous with impinging flow, while low-flow conditions are linked to slow recirculation. Our results suggest this assumption is oversimplified. High-flow regions can occur independently of impinging jets, such as near flow detachment points after passing through a hyperbolic patch, as seen in Fig. 6. While both impingement and detachment can occur on saddle-like patches, spherical-like patches are predominantly sites of impingement. This indicates that wall curvature, independent of global flow patterns, is the primary determinant of local hemodynamic behavior.

Meng et al. [24] hypothesized that these pathways lead to distinct wall phenotypes: “Type-II” (thick, atherosclerotic, yellow-whitish) and “Type-I” (thin, reddish). We investigated these phenotypes using the hemodynamic thresholds from our previous work [23], where low-flow patches were identified by $TAWSS < 5$ Pa and $OSI > 0.01$ Pa, and high-flow regions by $TAWSS > 10$ Pa and $OSI < 0.001$ Pa. These thresholds were established based on the averaged values reported by Furukawa et al. [52] and Cebal et al. [53] (see Fig. 12). Notably, white-thick (Type-II) patches were significantly more prevalent than red-thin (Type-I) patches across our sample ($p < 0.001$), irrespective of rupture status.

Excluding extreme outliers, saddle-like patches are more susceptible to the hemodynamic conditions favoring red-thin (Type-I) phenotypes, whereas

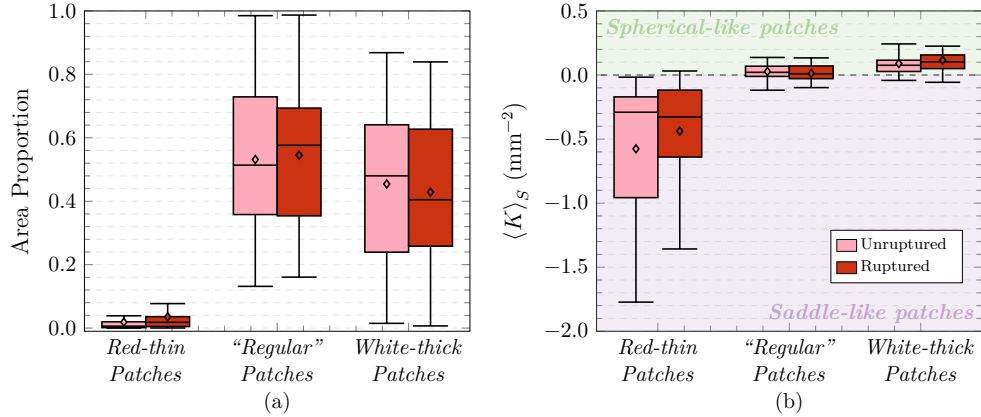


Figure 12: (a) Area proportion of abnormal-hemodynamic patches relative to the total aneurysm sac surface area; (b) Distribution of surface-averaged Gaussian curvature per abnormal-hemodynamics patches of type I (red-thin), II (white-thick), and also “regular” — neither Type-I nor Type-II.

spherical-like patches correlate with thick, atherosclerotic (Type-II) phenotypes. This aligns with findings suggesting that thin walls correlate with low OSI [54]. If validated in longitudinal studies, these relationships could facilitate the early identification of regions prone to specific wall phenotypes. Such information would be important for endovascular planning, as Type-I patches are thinner and significantly more susceptible to intraprocedural rupture [55, 56].

Limitations

Despite the robust correlations observed in this cohort, certain limitations merit discussion. First, Gaussian curvature calculations are inherently sensitive to numerical noise in discretized surfaces [37]. To minimize these errors, we utilized highly-refined surface meshes for all geometric computations. Furthermore, as our conclusions are derived from broad morphological regions

and surface-averaged metrics rather than point-wise values, it is unlikely that localized discretization noise influenced the primary findings of this study.

Second, regarding the physical modeling of blood flow, we assumed rigid vessel walls. While wall compliance and the resulting fluid-structure interaction can influence near-wall hemodynamics, the rigid-wall assumption is a well-established and validated standard for numerical investigations of intracranial aneurysms [57], particularly when focusing on time-averaged flow patterns. Future research incorporating moving boundaries may further elucidate the secondary effects of wall motion on the curvature-hemodynamic relationship established here.

Finally, the thresholds used to define low-flow and high-flow hemodynamics analyzed in Fig. 12b are relatively arbitrary. As detailed in our prior work [23], these values were synthesized from existing literature. To mitigate selection bias, we performed a parametric sensitivity study by independently varying the TAWSS and OSI thresholds. The fundamental structure of the distributions remained unchanged: saddle-like patches consistently favored high-flow conditions, while spherical-like patches favored low-flow environments, regardless of the specific cutoff values. This stability confirms that the relationship between curvature and hemodynamics is robust to threshold selection, further strengthening the conclusions of this study.

5. Conclusions

This study establishes local luminal curvature as a primary and independent determinant of the hemodynamic environment in CAs. By analyzing a large, heterogeneous cohort, we demonstrated that the relationship be-

tween surface morphology and hemodynamics remains robust, regardless of aneurysm type, location, or rupture status. Specifically, we show that saddle-like patches — typically found at the aneurysm neck — are preferentially associated with elevated TAWSS, low OSI, driven by intense near-wall vortical activity. Conversely, spherical-like regions, predominant at the dome, act as sites of flow impingement characterized by lower shear stress and higher OSI.

A key contribution of this work is the mechanistic link established between these geometric features and specific pathological wall phenotypes: saddle-like regions are prone to thin, reddish phenotypes, while spherical-like regions favor thick, atherosclerotic developments. These findings underscore the clinical potential of curvature-based mapping as a powerful, non-invasive tool. By leveraging readily available morphological data from routine imaging, this approach enables superior risk stratification — particularly when integrated into objective clinical scoring systems — more accurate prediction of wall vulnerability, and enhanced precision in planning endovascular interventions.

6. Acknowledgements

This work was supported by resources supplied by the Center for Scientific Computing (NCC/GridUNESP) of the São Paulo State University (UNESP) (www2.unesp.br/portal#!/gridunesp) and by the National Laboratory of Scientific Computing through the use of the SDumont supercomputer (projeto ID CFDIA). Funding: This research was supported by grants 2023/06609-9 and 2025/23522-0 of São Paulo Research Foundation (FAPESP).

References

- [1] M. H. M. Vlak, G. J. E. Rinkel, P. Greebe, A. Algra, Risk of rupture of an intracranial aneurysm based on patient characteristics: A case-control study, *Stroke* 44 (2013) 1256–1259. doi:10.1161/STROKEAHA.111.000679.
- [2] K. M. Saqr, Wall shear stress in the Navier-Stokes equation: A commentary, *Computers in Biology and Medicine* 106 (2019) 82–83. doi:10.1016/j.compbiomed.2019.01.012.
- [3] S. I. Tjoumakaris, R. Hanel, J. Mocco, M. Ali-Aziz Sultan, M. Froehler, B. B. Lieber, A. Coon, S. Tateshima, D. J. Altschul, S. Narayanan, K. El Naamani, P. Taussky, B. L. Hoh, P. Meyers, M. J. Gounis, D. S. Liebeskind, V. Volovici, G. Toth, A. Arthur, A. K. Wakhloo, for the ARISE I Consortium, ARISE I Consensus Review on the Management of Intracranial Aneurysms, *Stroke* 55 (2024) 1428–1437. doi:10.1161/STROKEAHA.123.046208.
- [4] E. L. Leemans, B. M. W. Cornelissen, C. H. Slump, Comparing Morphology and Hemodynamics of Stable-versus-Growing and Grown Intracranial Aneurysms, *American Journal of Neuroradiology* 40 (2019) 2102–2110. doi:10.3174/ajnr.A6307.
- [5] N. Juchler, S. Schilling, P. Bijlenga, S. Morel, D. Rufenacht, V. Kurtcuoglu, S. Hirsch, Shape irregularity of the intracranial aneurysm lumen exhibits diagnostic value, *Acta Neurochirurgica* 162 (2020) 2261–2270. doi:10.1007/s00701-020-04428-0.

- [6] M. R. Levitt, A. Aliseda, D. Fiorella, C. Sadasivan, One way to get there, *Journal of NeuroInterventional Surgery* 13 (2021) 401–402.
- [7] M. L. Raghavan, B. Ma, R. E. Harbaugh, Quantified aneurysm shape and rupture risk, *Journal of Neurosurgery* 102 (2005) 355–362. doi:10.3171/jns.2005.102.2.0355.
- [8] S. Dhar, M. Tremmel, J. Mocco, M. Kim, J. Yamamoto, A. H. Siddiqui, L. N. Hopkins, H. Meng, Morphology parameters for intracranial aneurysm rupture risk assessment, *Neurosurgery* 63 (2008) 185–196. doi:10.1227/01.NEU.0000316847.64140.81.
- [9] J. P. Greving, M. J. H. Wermer, R. D. Brown, A. Morita, S. Juvela, M. Yonekura, T. Ishibashi, J. C. Torner, T. Nakayama, G. J. E. Rinkel, A. Algra, Development of the PHASES score for prediction of risk of rupture of intracranial aneurysms: A pooled analysis of six prospective cohort studies, *Lancet* 13 (2014) 59–66. doi:10.1016/S1474-4422(13)70263-1.
- [10] N. Etminan, R. D. Brown, K. Beseoglu, S. Juvela, J. Raymond, A. Morita, J. C. Torner, C. P. Derdeyn, A. Raabe, J. Mocco, M. Korja, A. Abdulazim, S. Amin-Hanjani, R. Al-Shahi Salman, D. L. Barrow, J. Bederson, A. Bonafe, A. S. Dumont, D. J. Fiorella, A. Gruber, G. J. Hankey, D. M. Hasan, B. L. Hoh, P. Jabbour, H. Kasuya, M. E. Kelly, P. J. Kirkpatrick, N. Knuckey, T. Koivisto, T. Krings, M. T. Lawton, T. R. Marotta, S. A. Mayer, E. Mee, V. M. Pereira, A. Molyneux, M. K. Morgan, K. Mori, Y. Murayama, S. Nagahiro, N. Nakayama, M. Niemelä, C. S. Ogilvy, L. Pierot, A. A. Rabinstein, Y. B. Roos, J. Rinne, R. H. Rosenwasser,

- A. Ronkainen, K. Schaller, V. Seifert, R. A. Solomon, J. Spears, H.-J. Steiger, M. D. Vergouwen, I. Wanke, M. J. Wermer, G. K. Wong, J. H. Wong, G. J. Zipfel, E. S. Connolly, H. Steinmetz, G. Lanzino, A. Pasqualin, D. Rufenacht, P. Vajkoczy, C. McDougall, D. Hänggi, P. LeRoux, G. J. Rinkel, R. L. Macdonald, The unruptured intracranial aneurysm treatment score: A multidisciplinary consensus, *Neurology* 85 (2015) 881–889. doi:10.1212/WNL.0000000000001891.
- [11] H. Rajabzadeh-Oghaz, M. Waqas, S. S. Veeturi, K. Vakharia, M. K. Tso, K. V. Snyder, J. M. Davies, A. H. Siddiqui, E. I. Levy, H. Meng, A data-driven model to identify high-risk aneurysms and guide management decisions: The Rupture Resemblance Score, *Journal of Neurosurgery* 135 (2020) 9–16. doi:10.3171/2020.5.JNS193264.
- [12] J. Frösen, Smooth Muscle Cells and the Formation, Degeneration, and Rupture of Saccular Intracranial Aneurysm Wall—a Review of Current Pathophysiological Knowledge, *Translational Stroke Research* 5 (2014) 347–356. doi:10.1007/s12975-014-0340-3.
- [13] K. Fukazawa, F. Ishida, Y. Umeda, Y. Miura, S. Shimosaka, S. Matsushima, W. Taki, H. Suzuki, M. Bligh, Others, Using computational fluid dynamics analysis to characterize local hemodynamic features of middle cerebral artery aneurysm rupture points, *World Neurosurgery* 83 (2015) 80–86. doi:10.1016/j.wneu.2013.02.012.
- [14] J. Cezbral, E. Ollikainen, B. J. Chung, F. Mut, V. Sippola, B. R. Jahromi, R. Tulamo, J. Hernesniemi, M. Niemelä, A. Robertson, J. Frösen, Flow

- conditions in the intracranial aneurysm lumen are associated with inflammation and degenerative changes of the aneurysm wall, *American Journal of Neuroradiology* 38 (2017). doi:10.3174/ajnr.A4951.
- [15] A. J. Geers, H. G. Morales, I. Larrabide, C. Butakoff, P. Bijlenga, A. F. Frangi, Wall shear stress at the initiation site of cerebral aneurysms, *Biomechanics and Modeling in Mechanobiology* 16 (2017) 97–115. doi:10.1007/s10237-016-0804-3.
- [16] A. Lauric, J. Hippelheuser, M. G. Safain, A. M. Malek, Curvature effect on hemodynamic conditions at the inner bend of the carotid siphon and its relation to aneurysm formation, *Journal of Biomechanics* 47 (2014) 3018–3027. doi:10.1016/j.jbiomech.2014.06.042.
- [17] V. G. Ardakani, X. Tu, A. M. Gambaruto, I. Velho, J. Tiago, A. Sequeira, R. Pereira, Near-wall flow in cerebral aneurysms, *Fluids* 4 (2019) 1–27. doi:10.3390/fluids4020089.
- [18] V. Mazzi, D. Gallo, K. Calò, D. A. Steinman, U. Morbiducci, A revised and expanded unified theory linking wall shear stress and vorticity topologies to enable the interpretation of cardiovascular flow disturbances, *Physics of Fluids* 37 (2025) 031907. doi:10.1063/5.0253618.
- [19] S. F. Salimi Ashkezari, F. Mut, B. J. Chung, A. M. Robertson, J. R. Cebal, Hemodynamic conditions that favor bleb formation in cerebral aneurysms, *Journal of NeuroInterventional Surgery* 0 (2020) 1–6. doi:10.1136/neurintsurg-2020-016369.

- [20] Y. Karnam, F. Mut, A. K. Yu, B. Cheng, S. Amin-Hanjani, F. T. Charbel, H. H. Woo, M. Niemelä, R. Tulamo, B. R. Jahromi, J. Frösen, Y. Tobe, A. M. Robertson, J. R. Cebal, Description of the local hemodynamic environment in intracranial aneurysm wall subdivisions, *International Journal for Numerical Methods in Biomedical Engineering* 40 (2024) e3844. doi:10.1002/cnm.3844.
- [21] J. D. Humphrey, P. B. Canham, Structure, Mechanical Properties, and Mechanics of Intracranial Saccular Aneurysms, *Journal of Elasticity* 61 (2000) 49–81.
- [22] B. Ma, J. Lu, R. E. Harbaugh, M. L. Raghavan, Nonlinear Anisotropic Stress Analysis of Anatomically Realistic Cerebral Aneurysms, *Journal of Biomechanical Engineering* 129 (2007) 88–96. doi:10.1115/1.2401187.
- [23] I. Oliveira, P. Cardiff, C. Baccin, R. Tatit, J. Gasche, On the major role played by the lumen curvature of intracranial aneurysms walls in determining their mechanical response, local hemodynamics, and rupture likelihood, *Computers in Biology and Medicine* 163 (2023) 107178. doi:10.1016/j.combiomed.2023.107178.
- [24] H. Meng, V. M. Tutino, J. Xiang, A. Siddiqui, High WSS or Low WSS? Complex interactions of hemodynamics with intracranial aneurysm initiation, growth, and rupture: Toward a unifying hypothesis, *American Journal of Neuroradiology* 35 (2014) 1254–1262. doi:10.3174/ajnr.A3558.
- [25] J. Frösen, J. Cebal, A. M. Robertson, T. Aoki, Flow-induced, inflammation-mediated arterial wall remodeling in the formation and

- progression of intracranial aneurysms, *Neurosurgical Focus* 47 (2019) E21. doi:10.3171/2019.5.FOCUS19234.
- [26] Passerini, T. and Piccinelli, M. and Veneziani, A. and Antiga, L., aneurisk, <http://ecm2.mathcs.emory.edu/aneuriskweb/index>, 2021.
- [27] M. Piccinelli, S. Bacigaluppi, E. Boccardi, B. Ene-Iordache, A. Remuzzi, A. Veneziani, L. Antiga, Geometry of the Internal Carotid Artery and Recurrent Patterns in Location, Orientation, and Rupture Status of Lateral Aneurysms: An Image-Based Computational Study, *Neurosurgery* 68 (2011) 1270–1285. doi:10.1227/NEU.0b013e31820b5242.
- [28] K. Valen-Sendstad, M. Piccinelli, R. KrishnankuttyRema, D. A. Steinman, Estimation of Inlet Flow Rates for Image-Based Aneurysm CFD Models: Where and How to Begin?, *Annals of Biomedical Engineering* 43 (2015) 1422–1431. doi:10.1007/s10439-015-1288-5.
- [29] S. S. Shibeshi, W. E. Collins, The Rheology of Blood Flow in a Branched Arterial System with Three-Dimensional Model: A Numerical Study, *Applied Rheology* 15 (2005) 398–405. doi:10.1017/S1727719100002951.
- [30] J. G. Isaksen, Y. Bazilevs, T. Kvamsdal, Y. Zhang, J. H. Kaspersen, K. Waterloo, B. Romner, T. Ingebrigtsen, Determination of wall tension in cerebral artery aneurysms by numerical simulation, *Stroke* 39 (2008) 3172–3178. doi:10.1161/STROKEAHA.107.503698.
- [31] M. D. Ford, N. Alperin, S. H. Lee, D. W. Holdsworth, D. A. Steinman, Characterization of volumetric flow rate waveforms in the normal internal

- carotid and vertebral arteries, *Physiological Measurement* 26 (2005) 477–488. doi:10.1088/0967-3334/26/4/013.
- [32] Y. Hoi, B. A. Wasserman, Y. J. Xie, S. S. Najjar, L. Ferruci, E. G. Lakatta, G. Gerstenblith, D. A. Steinman, Characterization of volumetric flow rate waveforms at the carotid bifurcations of older adults, *Physiological Measurement* 31 (2010) 291–302. doi:10.1088/0967-3334/31/3/002.
- [33] C. Chnafa, P. Bouillot, O. Brina, M. Najafi, B. Delattre, M. Vargas, V. Pereira, D. Steinman, Errors in power-law estimations of inflow rates for intracranial aneurysm CFD, *Journal of Biomechanics* 80 (2018) 159–165. doi:10.1016/j.jbiomech.2018.09.006.
- [34] H. Jasak, *Error Analysis and Estimation for the Finite Volume Method with Applications to Fluid Flows*, 1996.
- [35] R. I. Issa, Solution of the implicitly discretised fluid flow equations by operator-splitting, *Journal of Computational Physics* 62 (1986) 40–65. doi:10.1016/0021-9991(86)90099-9.
- [36] I. L. Oliveira, G. B. Santos, J. L. Gasche, J. Miltzer, C. E. Baccin, Non-Newtonian Blood Modeling in Intracranial Aneurysm Hemodynamics: Impact on the Wall Shear Stress and Oscillatory Shear Index Metrics for Ruptured and Unruptured Cases, *Journal of Biomechanical Engineering* 143 (2021) 071006. doi:10.1115/1.4050539.
- [37] B. Ma, R. E. Harbaugh, M. L. Raghavan, Three-dimensional geometrical characterization of cerebral aneurysms., *Annals of Biomedical Engineering* 32 (2004) 264–273. doi:10.1023/B:ABME.0000012746.31343.92.

- [38] S. F. Salimi Ashkezari, F. J. Detmer, F. Mut, B. J. Chung, A. K. Yu, C. J. Stapleton, A. P. See, S. Amin-Hanjani, F. T. Charbel, B. Rezai Jahromi, M. Niemelä, J. Frösen, J. Zhou, S. Maiti, A. M. Robertson, J. R. Cebal, Blebs in intracranial aneurysms: Prevalence and general characteristics, *Journal of NeuroInterventional Surgery* 13 (2021) 226–230. doi:10.1136/neurintsurg-2020-016274.
- [39] X. He, D. N. Ku, Pulsatile Flow in the Human Left Coronary Artery Bifurcation: Average Conditions, *Journal of Biomechanical Engineering* 118 (1996) 74–82. doi:10.1115/1.2795948.
- [40] A. Surana, G. B. Jacobs, O. Grunberg, G. Haller, An exact theory of three-dimensional fixed separation in unsteady flows, *Physics of Fluids* 20 (2008) 107101. doi:10.1063/1.2988321.
- [41] A. M. Gambaruto, A. J. João, Flow structures in cerebral aneurysms, *Computers and Fluids* 65 (2012) 56–65. doi:10.1016/j.compfluid.2012.02.020.
- [42] A. Arzani, S. C. Shadden, Wall shear stress fixed points in cardiovascular fluid mechanics, *Journal of Biomechanics* 73 (2018) 145–152. doi:10.1016/j.jbiomech.2018.03.034.
- [43] A. Surana, O. Grunberg, G. Haller, Exact theory of three-dimensional flow separation. Part 1. Steady separation, *Journal of Fluid Mechanics* 564 (2006) 57–103. doi:10.1017/S0022112006001200.
- [44] V. Mazzi, D. Gallo, K. Calò, M. Najafi, M. O. Khan, G. De Nisco, D. A. Steinman, U. Morbiducci, A Eulerian method to analyze wall shear

- stress fixed points and manifolds in cardiovascular flows, *Biomechanics and Modeling in Mechanobiology* 19 (2020) 1403–1423. doi:10.1007/s10237-019-01278-3.
- [45] V. Mazzi, U. Morbiducci, K. Calò, G. De Nisco, M. Lodi Rizzini, E. Torta, G. C. A. Caridi, C. Chiastra, D. Gallo, Wall Shear Stress Topological Skeleton Analysis in Cardiovascular Flows: Methods and Applications, *Mathematics* 9 (2021) 720. doi:10.3390/math9070720.
- [46] J.-Z. Wu, H.-Y. Ma, M.-D. Zhou, *Vorticity and Vortex Dynamics*, Springer, 2006.
- [47] SciPy, SciPy Website, <https://www.scipy.org>, 2022. [Accessed 05-May-2022].
- [48] M. El Hassan, H. H. Assoum, V. Sobolik, J. Vétel, K. Abed-Meraim, A. Garon, A. Sakout, Experimental investigation of the wall shear stress and the vortex dynamics in a circular impinging jet, *Experiments in Fluids* 52 (2012) 1475–1489. doi:10.1007/s00348-012-1269-5.
- [49] N. C. Wild, K. V. Bulusu, M. W. Plesniak, Vortical Structures Promote Atheroprotective Wall Shear Stress Distributions in a Carotid Artery Bifurcation Model, *Bioengineering* 10 (2023) 1036. doi:10.3390/bioengineering10091036.
- [50] N. Varble, G. Trylesinski, J. Xiang, K. Snyder, H. Meng, Identification of vortex structures in a cohort of 204 intracranial aneurysms, *Journal of The Royal Society Interface* 14 (2017) 20170021. doi:10.1098/rsif.2017.0021.

- [51] J. M. Dolan, J. Kolega, H. Meng, High Wall Shear Stress and Spatial Gradients in Vascular Pathology: A Review, *Annals of Biomedical Engineering* 41 (2013) 1411–1427. doi:10.1007/s10439-012-0695-0.
- [52] K. Furukawa, F. Ishida, M. Tsuji, Y. Miura, T. Kishimoto, M. Shiba, H. Tanemura, Y. Umeda, T. Sano, R. Yasuda, S. Shimosaka, H. Suzuki, Hemodynamic characteristics of hyperplastic remodeling lesions in cerebral aneurysms, *PLOS ONE* 13 (2018) 1–11. doi:10.1371/journal.pone.0191287.
- [53] J. R. Cebal, F. Detmer, B. J. Chung, J. Choque-Velasquez, B. Rezai, H. Lehto, R. Tulamo, J. Hernesniemi, M. Niemela, A. Yu, R. Williamson, K. Aziz, S. Sakur, S. Amin-Hanjani, F. Charbel, Y. Tobe, A. Robertson, J. Frösen, Local hemodynamic conditions associated with focal changes in the intracranial aneurysm wall, *American Journal of Neuroradiology* 40 (2019) 510–516. doi:10.3174/ajnr.A5970.
- [54] H. Kimura, M. Taniguchi, K. Hayashi, Y. Fujimoto, Y. Fujita, T. Sasayama, A. Tomiyama, E. Kohmura, Clear Detection of Thin-Walled Regions in Unruptured Cerebral Aneurysms by Using Computational Fluid Dynamics, *World Neurosurgery* 121 (2019) e287–e295. doi:10.1016/j.wneu.2018.09.098.
- [55] S. Chen, Y. Kato, A. Kumar, G. Tan, D. Oguri, J. Oda, T. Watabe, S. Imizu, H. Sano, Z. Wang, Intraoperative rupture in the surgical treatment of patients with intracranial aneurysms, *Journal of Clinical Neuroscience* 34 (2016) 63–69. doi:10.1016/j.jocn.2016.01.045.

- [56] X.-L. Chen, Y. Chen, L. Ma, J.-K. Burkhardt, T. Wardell, C. Wang, G. Guo, S. Wang, Y.-L. Zhao, Translucent Appearance of Middle Cerebral Artery Bifurcation Aneurysms Is Risk Factor for Intraoperative Aneurysm Rupture During Clipping, *World Neurosurgery* 101 (2017) 149–154. doi:10.1016/j.wneu.2017.01.097.
- [57] J. R. Cebal, M. A. Castro, S. Appanaboyina, C. M. Putman, D. Millan, A. F. Frangi, Efficient pipeline for image-based patient-specific analysis of cerebral aneurysm hemodynamics technique and sensitivity, *IEEE Transactions on Medical Imaging* 24 (2005) 457–467. doi:10.1109/TMI.2005.844159.

Supplementary Material

Time-averaged Wall Shear Stress Gradient

To quantify the spatial variation of the TAWSS in our study, the TAWSSG field, TAWSSG, as defined by Geers et al. [15], was computed:

$$TAWSSG = (\nabla_t \overline{\tau_w}) \cdot \mathbf{p}, \quad (6.10)$$

where ∇_t is the tangential or surface gradient operator, given by:

$$\nabla_t \equiv \nabla - \hat{\mathbf{n}} (\hat{\mathbf{n}} \cdot \nabla), \quad (6.11)$$

with ∇ is the gradient operator in Cartesian coordinates and \mathbf{p} is the unit vector pointing in the time-averaged WSS vector direction:

$$\mathbf{p} = \frac{\int_0^{T_c} \boldsymbol{\tau}_w dt}{\left\| \int_0^{T_c} \boldsymbol{\tau}_w(\mathbf{x}, t) dt \right\|}. \quad (6.12)$$

In Fig. S1, we present the distribution of the TAWSSG for all aneurysms in our database, segregated by rupture-status groups as also the correlations between the TAWSSG and the surface-averaged Gaussian curvature.

Flow Temporal Evolution

To illustrate the temporal evolution of the flow structures and wall shear stress patterns in CAs, we present in Fig. S2 the evolution of the λ_2 isosurface, the WSS magnitude, and λ_2 field over the cardiac cycle for a representative CA case (case C0002 from the Aneurisk database) at three instants of the cardiac cycle.

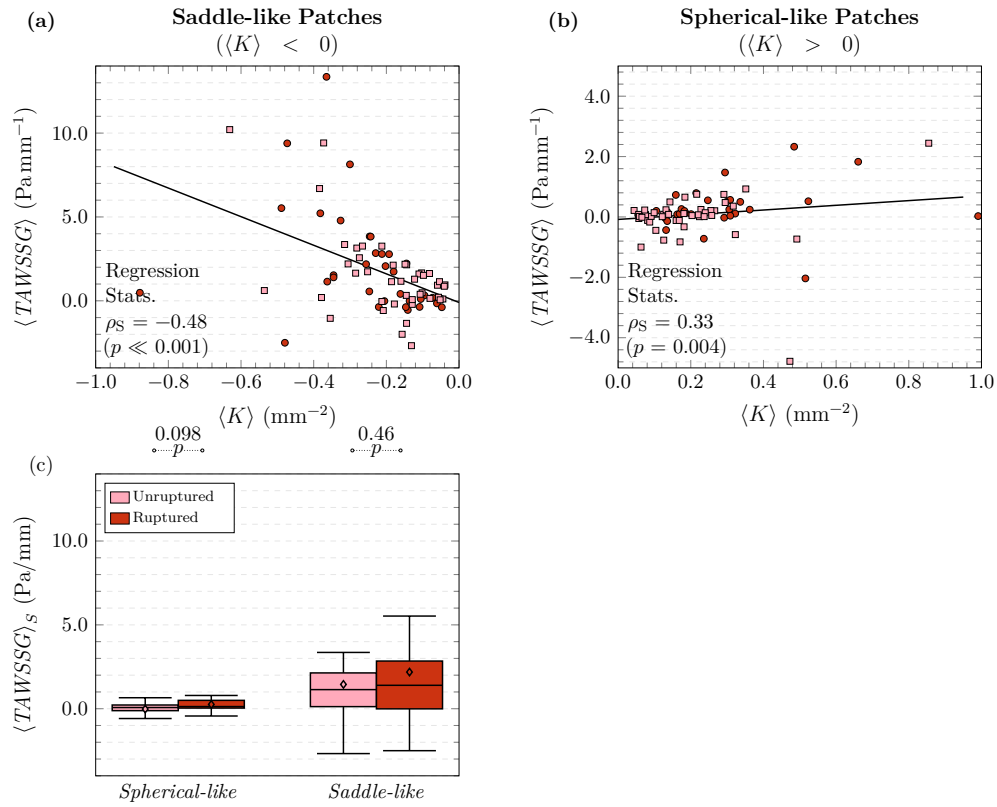


Figure S1: (a) and (b) Correlations between the TAWSSG and the surface-averaged Gaussian curvature and (c) distribution of the TAWSSG for all aneurysms in our database, segregated by rupture-status groups.

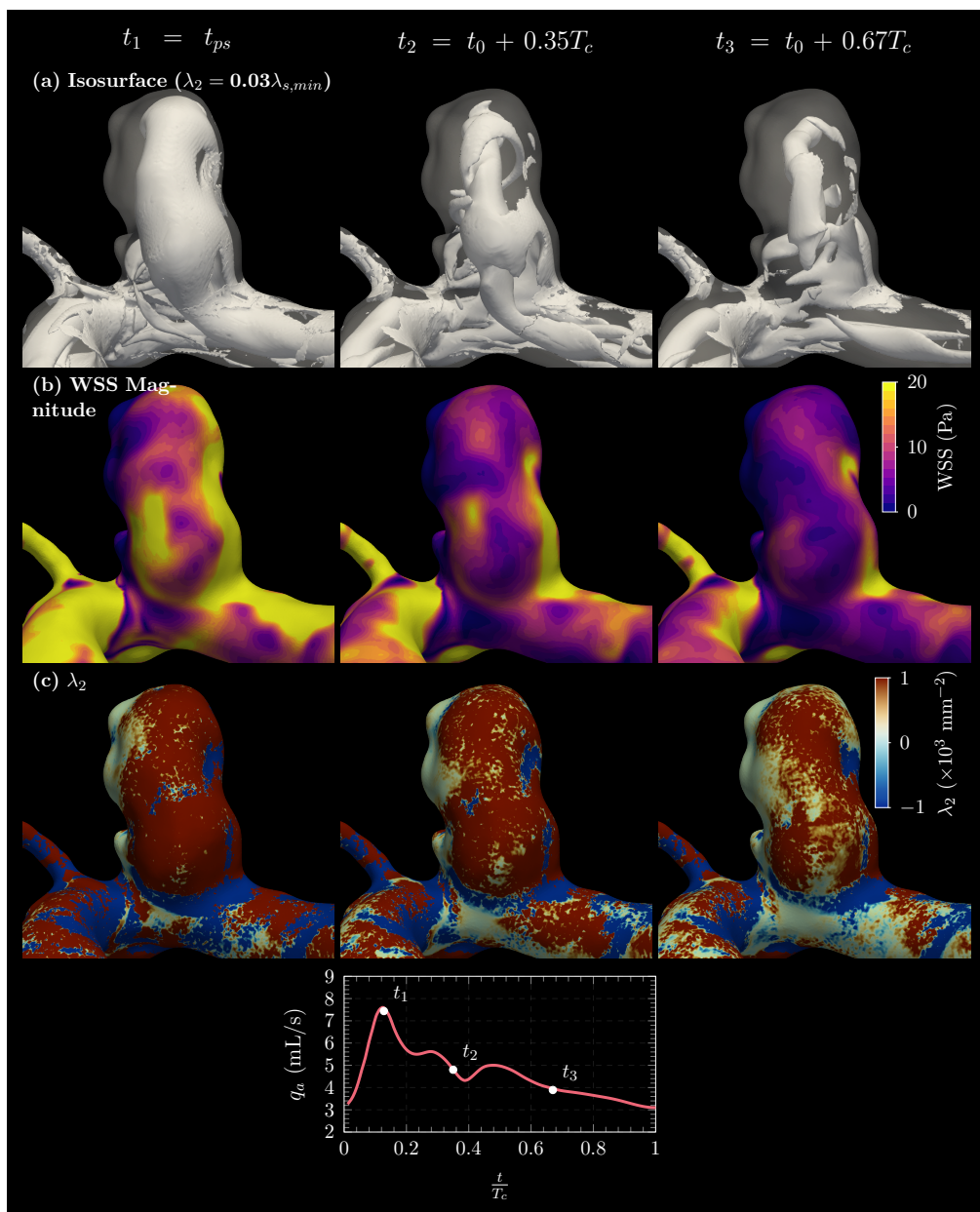


Figure S2: Evolution of the (a) λ_2 isosurface, (b) WSS magnitude, and (c) λ_2 field over the cardiac cycle for a representative CA case (case C0002 from the Aneurisk database) at three instants of the cardiac cycle.